

# Mechanical properties and mesoscopic analysis of rock-backfill-rock composite sample under dynamic loading

**D Zheng** *Beijing General Research Institute of Mining and Metallurgy, China*

**LJ Guo** *Beijing General Research Institute of Mining and Metallurgy, China*

**GS Liu** *Beijing General Research Institute of Mining and Metallurgy, China*

**XC Yang** *Beijing General Research Institute of Mining and Metallurgy, China*

**S Wu** *Beijing General Research Institute of Mining and Metallurgy, China*

## Abstract

*During ore pillar excavation, the impact load of deep hole blasting does not act directly in the cemented paste backfill (CPB), which first acts within the ore pillar and then transfers the blast energy to the CPB and the adjacent ore. Therefore, it is a key issue to investigate the stability of the rock-backfill composite under dynamic loading. The paper prepared rock-backfill-rock (RBR) composite samples and conducted the Split Hopkinson Pressure Bar (SHPB) dynamic test with different impact amplitude. The dynamic uniaxial strength characteristics, mechanical characteristics, and failure modes of RBR composite samples under different impact velocities were analysed. The experimental results showed that the dynamic uniaxial compressive strength of the RBR sample increases first and then decreases with the increase of the average strain rate. With the rise in the average strain rate, the fragmentation degree of the RBR sample is deepened. According to the computerised tomography (CT) test results, the rock fails mainly in shear. Moreover, damage occurs at the interface between the CPB and the rock near the incident bar. It is primarily manifested as a ring-layered crack, resulting in its separation from the rock near the incident bar. The results of the study can further guide the stability of the backfill stope during the ore pillar extraction process.*

**Keywords:** *mine backfill; cemented backfill; rock-backfill; mechanical properties; computerised tomography*

## 1 Introduction

Mining methods that require backfilling utilise mine waste to fill underground voids created by mining activities, thereby reducing surface waste. However, the ability of the cement paste backfill (CPB) as an essential structure for mine safety does not depend solely on its mechanical properties (Zvarivadza & Sengani 2018). It is also influenced by the overall structure of the ‘rock-backfill-rock’ (RBR) combination. The internal stress of RBR is complex, which leads to a change in its bearing capacity and more complex failure characteristics. The difference in the ore’s stability and hardness coefficients means there is also a significant difference in the mutual stress effect between the CPB and the ore. Especially for mining fractured ore in a deep high-stress environment, the CPB is susceptible to deformation by the stress transfer of the fractured ore and exhibits noticeable differences in mechanical properties (Guo et al. 2022).

For the influence of the interaction between the CPB and the host rock, many researchers have also carried out relevant studies through physical tests and numerical simulations (Tan et al. 2020). In most cases, the

statics behaviour of CPB and host rock was studied with sublevel open stoping as the research background (Ping et al. 2019; Wang & Fu 2021; Wu et al. 2013). Ercikdi et al. (2009) argue that the dynamic matching design strength of the CPB and host rock must meet the self-stability requirements of CPB and the three-way stress strength criterion under multi-factor conditions. Nasir et al. (2008) investigated the shear deformation of the CPB on the contact surface between the CPB and the host rock. Kun et al. (2018) used temperature as the main influencing factor to carry out shear experiments of the CPB-rock combination model under three different temperature conditions to explore the mechanical properties of the CPB-rock interface. Song et al. (2017) compared the triaxial tests of the whole rock column and rock column wrapped with CPB. They found a rebound trend after the failure of rock-CPB samples, which proved that rock-CPB as a system interacted with each other and participated in the support effect together.

Based on the dynamic failure of many composite systems in practical engineering, many scholars have also conducted SHPB tests of composite structures. For example, Han et al. (2022) found that the cement mortar layer can serve as a buffer during the deformation of composite samples by a split Hopkinson pressure bar system. Tarfaoui et al. (2013) investigate the compressive loading at high strain rates on composite naval and aeronautic structures. Yang et al. (2019) prepared samples of red sandstone and grey sandstone complexes and theoretically analysed their mechanical characteristics and strength conditions. They found that red sandstone with low wave impedance had greater failure strength.

The authors of this study proposed preparing an RBR sample to carry out the SHPB test to explore the failure characteristics of RBR. The complete samples after the SHPB test were selected for micro-CT scanning, and the failure characteristics and microscopic failure modes of rock and backfill were analysed, respectively. The research results can further guide the stability of the backfill stope during pillar mining.

## 2 Materials and method

### 2.1 Material characterisation

Materials used in this work consist of unclassified tailings, binders, and water. The unclassified tailings used in the test were from a gold mine in China, and the density of the tailings was  $2.34 \text{ g/cm}^3$  with a weight-specific surface area of  $39.595 \text{ m}^2/\text{kg}$ . Before the test, the unclassified tailings were dried, and then the particle size was analysed by the LS-POP laser particle size analyser. Figure 1 shows the particle size distribution curve of the unclassified tailings. The  $d_{50}$  of the unclassified tailings is  $321.3 \mu\text{m}$ , coarse tailings according to the tailings distribution classification (Cao et al. 2021), and the inhomogeneity coefficient  $C_u=5$  for the unclassified tailings.

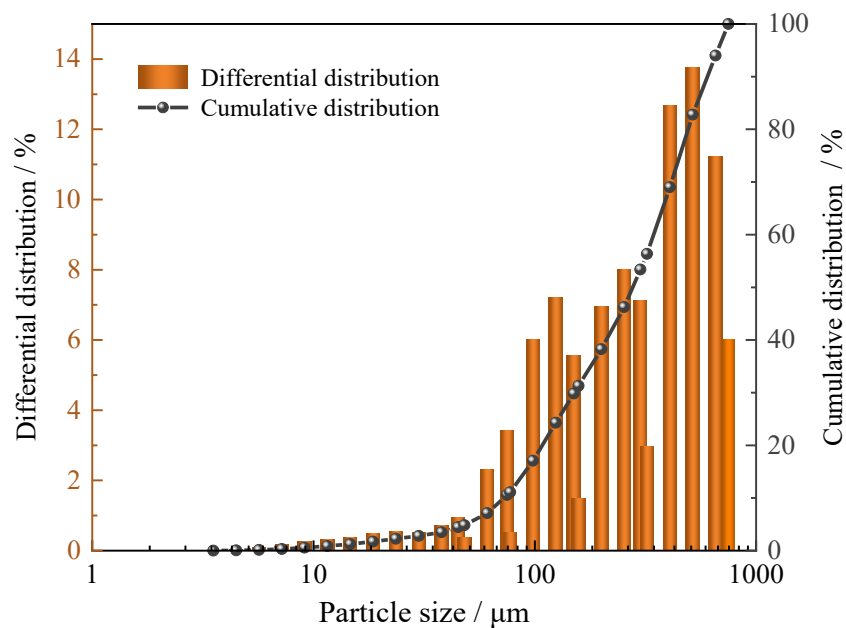


**Figure 1** Unclassified tailings particle size distribution curve

Binders are ordinary Portland cement with nominal 28-day compressive strength of 42.5 MPa (P.O. 42.5R). The chemical composition is shown in Table 1. The active component CaO accounted for 35.4wt %, followed by SiO<sub>2</sub>, accounting for 17.1wt %. The water is ordinary tap water. The rock is granite with ordinary medium grain.

**Table 1** Chemical composition analysis of cement

Chemical composition	CaO	SiO <sub>2</sub>	SO <sub>3</sub>	Al <sub>2</sub> O <sub>3</sub>	Fe <sub>2</sub> O <sub>3</sub>	TiO <sub>2</sub>	K <sub>2</sub> O	MnO
Content / wt. %	35.40	17.10	3.21	2.39	2.19	0.56	0.44	0.10

## 2.2 RBR Sample preparation

Dynamic compressive strength of CPB has an apparent size effect (Mitchell et al. 2011). To ensure the sample's one-dimensional stress propagation and stress balance during the dynamic load test, scholars suggest that the diameter of the sample should be like the diameter of the incident bar. The height-to-diameter ratio of the sample should be 0.5 to 1 (Zhang et al. 2009).

The design sample in this paper is a rock-backfill-rock three-layer combination sample. Due to the difficulty of processing, the height-to-diameter ratio of the RBR sample is chosen to be 1, i.e., the height of the RBR is 50 mm, and the diameter is 50 mm. The height of the rock is 15 mm, and the height of the CPB is 20 mm. The cement-sand ratio of the CPB is 1:4, the slurry concentration is 75%, and the curing age is 28 days.

Nunes et al. (2022) have shown that epoxy resin glue can characterise rock mechanical behaviour well. Therefore, the test used epoxy resin glue to combine the CPB with rock. The preparation process of the RBR sample is shown in Figure 2.

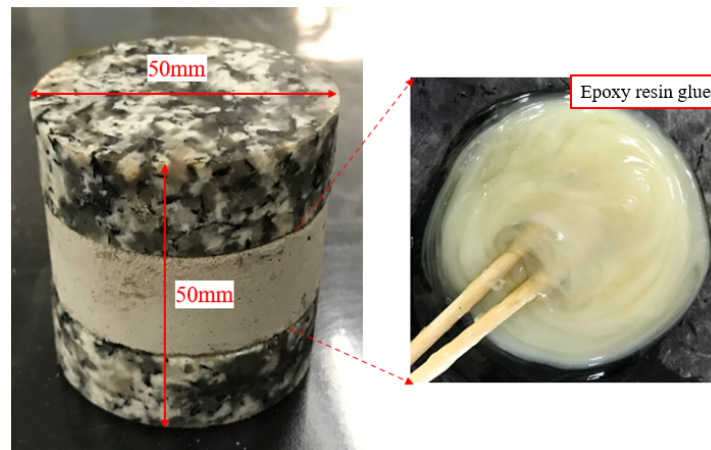


**Figure 2 RBR sample preparation process**

The SHPB test was carried out on the RBR sample with different impact amplitudes of 50, 75, 100, 125, 150, and 175 mV, and three sets of tests were repeated for each impact amplitude. Figure 3 shows all the RBR samples prepared in this paper. The test number is named “Y-Impact Amplitude - Serial number”; for example, Y-100-2 represents the second test of the RBR sample at an impact amplitude of 100 mV.



**Figure 3 RBR samples**

## 2.3 Experimental devices and procedures

### 2.3.1 Split Hopkinson Pressure Bar test

The SHPB test system consists of a nitrogen cylinder, an emission cavity, a spindle-shaped impact head, an incident bar, a transmission bar, a pressure device, an absorption device, a super dynamic strain gauge, a timer, an oscilloscope, a computer, and so on. The pressure bar in the SHPB test device is made of 40Cr alloy steel, has a density of  $7800 \text{ kg/m}^3$ , a wave speed of  $5200 \text{ m/s}$ , and a diameter of  $50 \text{ mm}$  (Zheng et al. 2021).

### 2.3.2 Computed tomography scanning test

This paper’s X-ray computed tomography (CT) testing system is German YXLON high-resolution testing equipment. This system is a “double source and double detector,” “double source,” that is, 225 kV microfocus and 450 kV light source, and a “double detector” for the flat plate and line array detector. A 225 kV microfocus micro-CT light source with continuous rotational scanning (2D/3D scanning) and a spatial distribution rate of  $23 \text{ Lp/mm}$  was used in this paper (Zheng et al. 2022).

### 2.3.3 Standard sieve

A set of standard sieves was selected to sieve the broken pieces of RBR samples after the damage of the SHPB test. The aperture sizes of the standard sieve are 9.5 mm, 4.75 mm, 2.36 mm, 1.18 mm, and 0.6 mm, and Figure 4 shows the standard sieve diagram. Since the samples were scattered around after the SHPB test, 100% of the damaged samples could not be collected. The individual sieving results were not weighed and could not be quantitatively analysed. Therefore, the macroscopic damage morphology of the RBR samples was mainly described qualitatively.



**Figure 4** A set of standard sieves

### 2.4 Split Hopkinson Pressure Bar test principle

According to the theory of one-dimensional elastic stress wave, it is known that there are the following relations between the two faces of the incident bar and the transmission bar in contact with the sample (Pang et al. 2010) :

$$U_1 = c_0 \int_0^t (\varepsilon_i - \varepsilon_r) dt \quad (1)$$

$$U_2 = c_0 \int_0^t \varepsilon_t dt \quad (2)$$

Where:

$U_1$  = displacement of the face of the sample connected to the incident bar;

$U_2$  = displacement of the face of the sample connected to the transmission bar;

$c_0$  = elastic wave velocity in the pressure bar;

$\varepsilon_i$  = strain in the bar corresponding to the incident wave;

$\varepsilon_r$  = strain in the bar corresponding to the reflected wave;

$\varepsilon_t$  = strain in the bar corresponding to the transmission wave.

Suppose the initial length of the sample is  $l_0$ . Then the average strain in the sample is:

$$\varepsilon(t) = \frac{u_1 - u_2}{l_0} = \frac{c_0}{l_0} \int_0^t (\varepsilon_i - \varepsilon_r - \varepsilon_t) dt \quad (3)$$

The average strain rate obtained by taking the derivative of equation (3) is:

$$\dot{\varepsilon} = \frac{c_0}{l_0} (\varepsilon_i - \varepsilon_r - \varepsilon_t) \quad (4)$$

The pressure of the sample and the contact surface of the incident and transmission bar are as follows:

$$F_1 = AE(\varepsilon_i + \varepsilon_r) \quad (5)$$

$$F_2 = AE\varepsilon_t \quad (6)$$

Where:

$F_1$  = pressure at the contact surface of the incident bar;

$F_2$  = pressure at the contact surface of the transmission bar;

$A$  = section area of the bar;  $E$  is the elastic modulus of the bar.

When the force on the two ends of the sample is balanced, there are:

$$F_1 = F_2 \quad (7)$$

According to Equations (5) and (6), we have:

$$\varepsilon_i + \varepsilon_r = \varepsilon_t \quad (8)$$

It can be obtained from Equation (8) that:

$$\sigma = \frac{AE}{A_0} \varepsilon_t \quad (9)$$

Where:

$A_0$  = section area of the sample.

$$\varepsilon = -\frac{2c_0}{l_0} \int_0^t \varepsilon_r dt \quad (10)$$

$$\dot{\varepsilon} = -\frac{2c_0}{l_0} \varepsilon_r \quad (11)$$

According to the waveform data recorded on the incident bar and transmission bar in the SHPB test, the stress, strain, and average strain rate of the sample can be calculated by equations (9), (10), and (11).

### 3 Results and discussion

#### 3.1 SHPB test waveforms of RBR

The initial waveforms of the RBR samples at different impact amplitudes of 50, 75, 100, 125, 150, and 175 mV are shown in Figure 5. According to the initial waveform diagram, the magnitudes of the incident and reflected waves are similar in magnitude and opposite in direction. The amplitude of the transmission wave is very small, which means that the stress wave is received less by the transmission bar after passing through the RBR sample, only a small part of the energy passes through the RBR sample, and most of the energy is reflected.

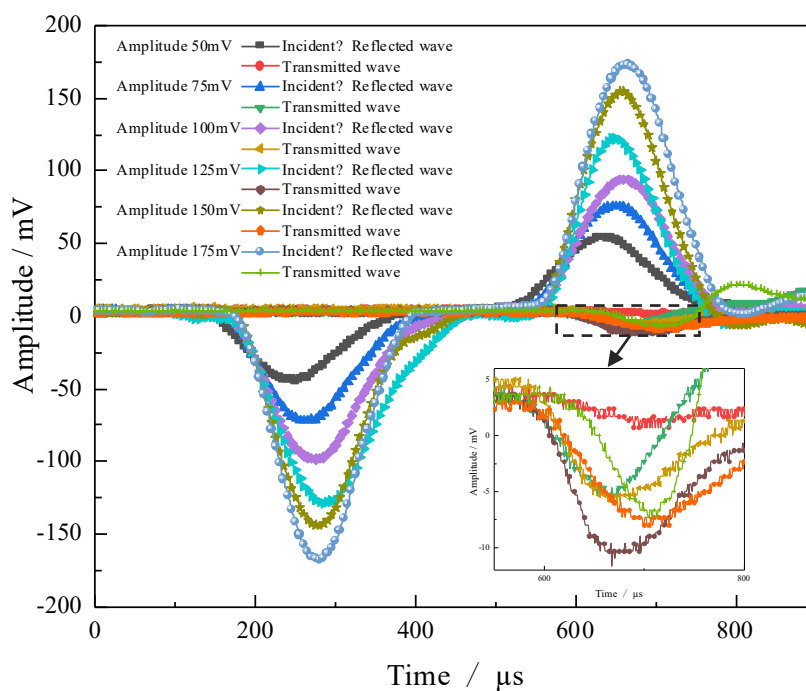


**Figure 5** Initial waveform of RBR samples

This effect is due to the significant difference in wave impedance between the granite, CPB, and metal bar of the SHPB device. The variation of wave impedance strongly influences the propagation of stress waves. When the stress wave propagates into two media, the wave impedance of the media differs. Therefore, regardless of increasing or decreasing, the energy of the incident wave cannot be fully propagated from one medium to the other. When the stress wave propagates in the RBR samples, it undergoes several wave impedance changes, so the transmission wave energy is minimal.

#### 3.2 Dynamic uniaxial compressive strength of RBR

According to the SHPB test principle equation in Section 2.4, the SHPB test results of RBR samples are calculated, as illustrated in Table 2 Statistical table of SHPB test results of RBR samples.

**Table 2 SHPB test results of RBR samples**

Sample number	Impact amplitude / mV	Impact velocity / m·s <sup>-1</sup>	average strain rate / s <sup>-1</sup>	Dynamic uniaxial compressive strength / MPa
Y-50-3	45	3.68	9.06	1.27
Y-75-2	71	5.77	17.89	3.73
Y-100-1	98	7.49	23.33	5.93
Y-125-2	129	10.72	41.72	10.72
Y-150-2	146	12.84	60.05	7.22
Y-175-1	170	16.06	76.92	6.08

Figure 6 shows the relationship between the average strain rate of RBR samples and impact velocity and dynamic uniaxial compressive strength. With the increase of the average strain rate, the impact velocity of the RBR sample increases, reaching a maximum of 16.06m/s. The dynamic uniaxial compressive strength of the RBR sample increases first and then decreases with the increase of the average strain rate. When the average strain rate is less than 41.72s<sup>-1</sup>, the dynamic uniaxial compressive strength of the RBR sample increases rapidly with the increase of the average strain rate, and the maximum is 10.72MPa. When the average strain rate is greater than 41.72s<sup>-1</sup>, the dynamic uniaxial compressive strength of the RBR sample decreases, and the decreasing trend tends to be gentle. When the impact velocity is 16.06m/s, and the average strain rate is 76.92s<sup>-1</sup>, the dynamic uniaxial compressive strength of the RBR is reduced to 6.08MPa. Energy dissipation occurs after the stress wave passes through the four interfaces of the incident bar and rock, rock and CPB, CPB and rock, and rock and transmission bar. Therefore, the energy received by the transmission bar is very low. Energy escapes from the interface, separating the parts of the assembly.

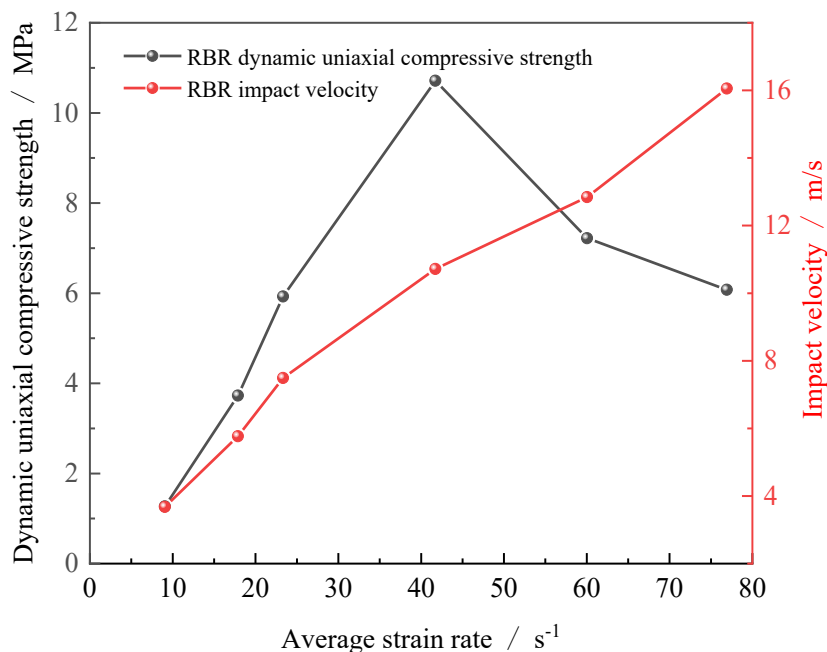


**Figure 6 The relationship between average strain rate and impact velocity and dynamic uniaxial compressive strength of RBR samples**

### 3.3 Macro failure mode analysis of RBR

Figure 7 shows the photos of the RBR sample after impact crushing, where (c) to (f) are the results after screening with the sieve. It can be seen from Figure 7 (a) that when the impact amplitude is 50 mV, the rock near the incident bar of the RBR sample is separated along the interface adjacent to the CPB. In contrast, the CPB is not separated from the rock near the transmission bar. All parts of the CPB and rock remain intact. During the falling process, the edge of the CPB sample is peeled off with debris. The analysis shows that when the stress wave passes into the RBR sample, energy dissipation occurs at the interface between the first rock and the CPB, resulting in the separation of the composite. The residual energy did not cause obvious macroscopic damage to the rock and CPB.

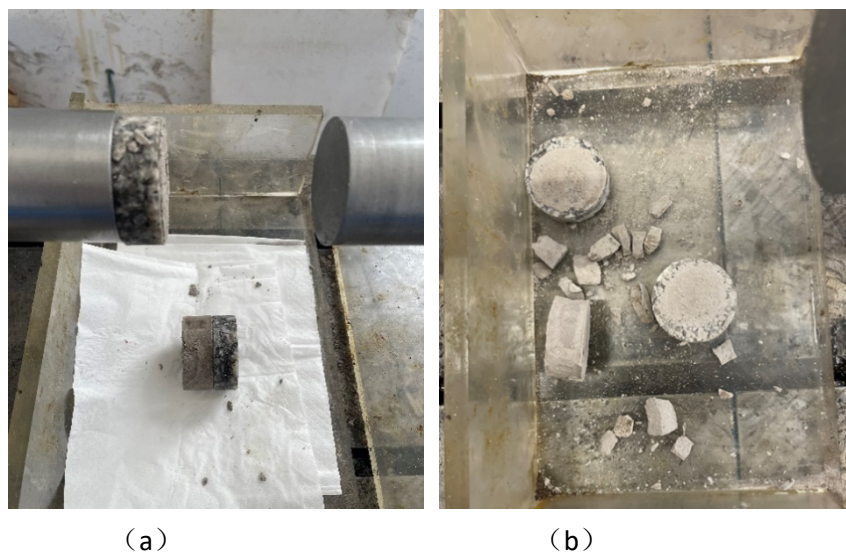
Figure 7 (b) shows the failure of the RBR sample when the impact amplitude is 75 mV and the CPB is separated from the rocks on both sides. The CPB sample was damaged, and some crushed particles fell around, but most of the CPB was intact and still had residual strength. The rock is partially intact with no macroscopic surface damage, which indicates that the energy dissipation of the stress wave at the interface between rock and CPB leads to the separation of RBR samples, and the reflected wave does not cause obvious damage to the rock, while the transmission wave enters the CPB and causes slight damage.

When the impact amplitude increases to 100 mV, the RBR samples are entirely separated, the rock part also has visible damage, and the CPB samples are broken without residual strength. Figure 7 (c) shows that the rock fragmentation degree is greater than the maximum value of the standard screen of 9.5 mm. The fragmentation degree of CPB is mostly greater than 9.5 mm and 4.75-9.5 mm.

When the impact amplitude increases to 125 mV, the screening diagram of RBR samples after failure is shown in Figure 7 (d). There is no significant difference in the fragmentation degree of CPB. However, the powder of the CPB less than 0.6 mm increased significantly, and visible damage occurred on both sides of the rock.

Figure 7 (e) shows the failure of the RBR sample under the impact amplitude of 150 mV. The fragmentation degree of CPB larger than 9.5 mm decreased obviously, and the powder CPB increased obviously. The fragmentation degree after rock failure is still greater than 9.5 mm.

We can see from Figure 7 (f) that when the impact amplitude increases to 175 mV, the rock damage increases significantly, and the rock sample cannot be restored. The rock lumpiness appears between 4.75-9.5 mm and 1.18-2.36 mm. The fragmentation degree of CPB is also significantly reduced.





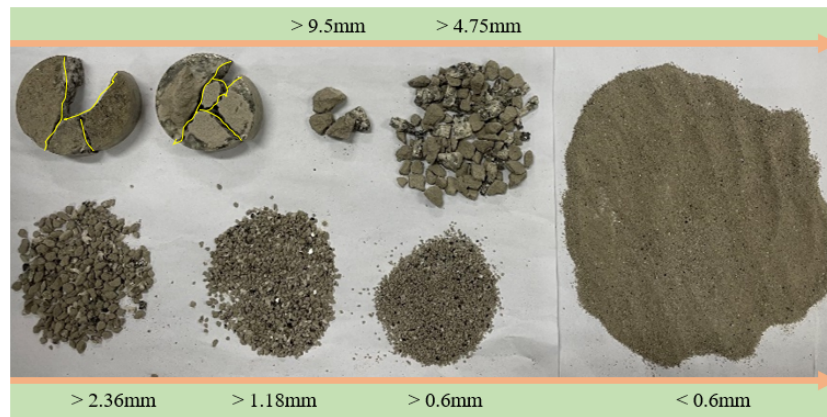
(c)



(d)



(e)



(f)

**Figure 7 Sieving of RBR samples after SHPB test. Impact amplitude (a)50 mV; (b)75 mV; (c)100 mV; (d)125 mV; (e)150 mV; (f)175 mV**

### 3.4 Micro failure mode analysis of RBR

According to the damage figures of the RBR samples after the SHPB test in Section 3.3, the RBR samples with an impact amplitude of 50 mV are relatively complete, which can be used for micro-CT scanning tests. Further, CT nondestructive testing was used to observe the internal damage of RBR samples, and three-dimensional (3D) reconstruction technology was used to visualise the RBR samples.

Figure 8 shows the 3D reconstruction of the RBR sample. We can directly observe that the rock near the incident bar separates from the RBR sample, and microcracks occur on its surface, but they are not fractured at the macro level. Moreover, the specific morphology of cracks at corresponding positions is shown on the right. The right side shows the specific morphology of the crack at the corresponding position. There is no apparent damage on the rock outside near the transmission bar. Micro cracks are on the rock's upper end, side, and inside. However, the microcrack width is minimal and does not penetrate through the rock, so its macroscopic morphology is complete. According to the crack morphology, the rock is mainly a shear failure. Damage occurs at the interface between the CPB and the rock near the incident bar, primarily manifested as a ring-layered crack, resulting in its separation from the rock near the incident bar. There is no damage inside the CPB. There is no apparent damage on the rock surface near the end of the transmission bar, but microcracks are inside.

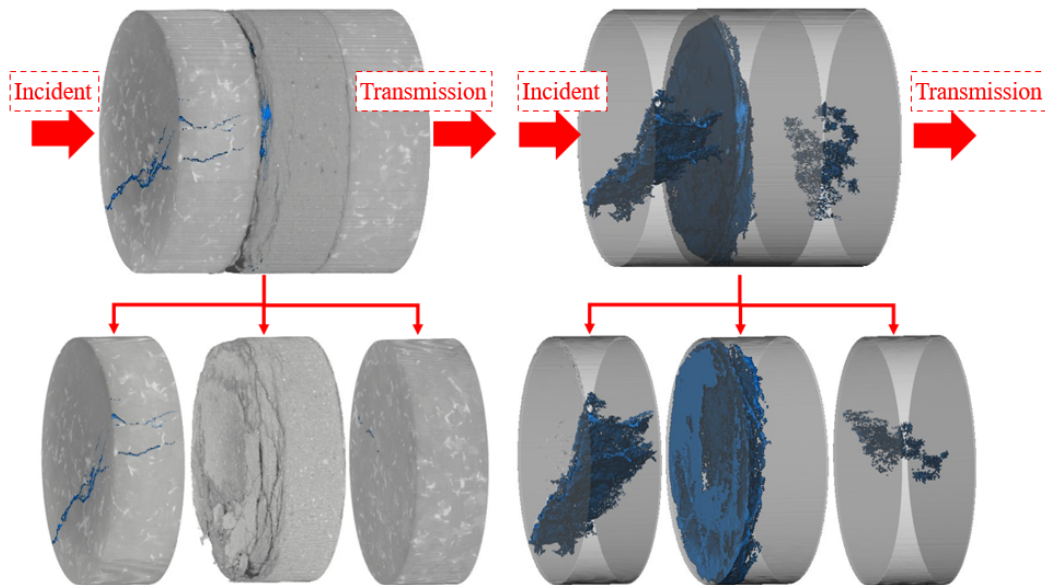


**Figure 8** 3D reconstruction of RBR

When the stress wave passes through the RBR sample and reaches the transmission bar, the energy carried by the stress wave mainly acts on the interface between the rock and the CPB, resulting in the separation of the rock and the CPB at the incident bar. In addition, shear microcracks are formed in the rock near the incident bar. In this case, no apparent damage is caused to the interior of the CPB, only lamellar fracture occurs near the end face, and microcracks appear in the rock at the distal end of the transmission bar. This shows that most energy escapes from the interface between rock and CPB when dynamic load occurs. The rock near the incident bar is damaged by the superposition of the incident wave and the reflected wave energy of the CPB, but the transmission wave does not cause apparent damage to the CPB.

## 4 Conclusion

In this paper, RBR samples were prepared, and the SHPB test was carried out under different impact amplitudes. The microscopic failure of RBR samples with impact amplitudes of 50 mV was obtained by CT scanning and three-dimensional reconstruction technology, and the following conclusions were obtained:

- (1) In the initial waveform of the RBR sample, the directions of the incident wave and the reflected wave are opposite, the impact amplitude is similar, and the transmission wave amplitude is minimal.
- (2) The impact velocity of RBR samples is positively correlated with the average strain rate, and the strain rate effect exists in the RBR samples. When the average strain rate is  $41.72 \text{ s}^{-1}$ , the maximum dynamic uniaxial compressive strength is 10.72 MPa. When the average strain rate is greater than  $41.72 \text{ s}^{-1}$ , the strain rate effect decreases.
- (3) Under a low strain rate (less than  $17.89 \text{ s}^{-1}$ ), the stress waves mainly dissipate at the interface, and the incident waves dissipate at the interface between the rock and the CPB. They resulted in the separation of the rock and the CPB. The reflected wave and transmission wave do not cause significant damage to the rock and the CPB. With the increase of the impact amplitude, the fragmentation degree of the CPB in the middle of the RBR decreases gradually, the crushed particles increase, and the granite is broken into small pieces from the complete form.
- (4) According to micro-CT results, after the SHPB test with an impact amplitude of 50 mV, significant amounts of damage in the RBR samples occur in the rock at the incident bar, which produces shear cracks. There is no damage inside the CPB, and an annular crack occurs at the end. There is no damage on the rock surface at the transmission bar, and microcracks are initiated inside.

## Acknowledgements

Financial support from the National Key Research and Development Program of China (Grant No. 2021YFC2900600 & 2022YFE0129200 & 2021YFC2902102) and the National Nature Fund Project (Grant No. 52274122) is gratefully acknowledged.

## References

- Cao, S, Yilmaz, E, Yin, Z, Xue, G, Song, W & Sun, L 2021, 'CT scanning of internal crack mechanism and strength behavior of cement-fiber-tailings matrix composites', *Cement and Concrete Composites*, vol. 116, article no. 103865, <https://doi.org/10.1016/j.cemconcomp.2020.103865>
- Ercikdi, B, Cihangir, F, Kesimal, A, Deveci, H & Alp, O 2009, 'Utilization of industrial waste products as pozzolanic material in cemented paste backfill of high sulphide mill tailings', *Journal of Hazardous Materials*, vol. 168, no. 2-3, pp. 848-856, <https://doi.org/10.1016/j.jhazmat.2009.02.100>
- Guo, L, Peng, X, Zhao, Y, Liu, G, Tang, G & Pan, A 2022, 'Experimental study on direct tensile properties of cemented paste backfill', *Advances in Design and Implementation of Cementitious Backfills (ADICB)*, vol. 9, article no. 864264, <https://doi.org/10.3389/fmats.2022.864264>
- Han, Z, Li, D & Li, X 2022, 'Dynamic mechanical properties and wave propagation of composite rock-mortar specimens based on SHPB tests', *International Journal of Mining Science and Technology*, vol. 32, no. 4, pp. 793-806, <https://doi.org/10.1016/j.ijmst.2022.05.008>
- Kun, F & Fall, M 2018, 'Effects of curing temperature on shear behaviour of cemented paste backfill-rock interface', *International Journal of Rock Mechanics and Mining Sciences*, vol. 112, pp. 184-192, <https://doi.org/10.1016/j.ijrmms.2018.10.024>
- Mitchell, MR, Link, RE, Wang, S, Zhang, M & Quek, ST 2011, 'Effect of specimen size on static strength and dynamic increase factor of high-strength concrete from SHPB test', *Journal of Testing and Evaluation*, vol. 39, no. 5, paper ID. JTE103370.
- Nunes, PDP, Marques, EAS, Carbas, R.JC, Akhavan-Safar, A & Da Silva, LFM 2022, 'Quasi-static and intermediate test speed validation of SHPB specimens for the determination of mode I, mode II fracture toughness of structural epoxy adhesives', *Engineering Fracture Mechanics*, vol. 262, article no. 108231, <https://doi.org/10.1016/j.engfracmech.2021.108231>
- Nasir, O & Fall, M 2008, 'Shear behaviour of cemented pastefill-rock interfaces', *Engineering Geology*, vol. 101, no. 3-4, pp. 146-153, <https://doi.org/10.1016/j.enggeo.2008.04.010>
- Pang, B, Yao, Z & Gai, B 2010, 'Strain rate design in SHPB test', in *Fourth International Conference on Experimental Mechanics*, SPIE, vol. 7522, pp. 276-282, <https://doi.org/10.1117/12.850894>
- Ping, L, Cong, L, Zhang, J, Yong, C & Qi, N 2019, 'Experimental study on strength of cemented rock-tailings backfill', *IOP Conference Series: Earth and Environmental Science*, IOP Publishing, vol. 227, article no. 52028, <https://doi.org/10.1088/1755-1315/227/5/052028>
- Song, W, Zhu, P, Qi, W & Tang, Y 2017, 'Coupling mechanism of rock-backfill system under triaxial compression', vol. 34, no. 3, pp. 573-579.
- Tan, Y, Davide, E, Zhou, Y, Song, W & Meng, X 2020, 'Long-term mechanical behavior and characteristics of cemented tailings backfill through impact loading', *International Journal of Minerals, Metallurgy and Materials*, vol. 27, no. 2, pp. 140-151, <https://doi.org/10.1007/s12613-019-1878-6>
- Tarfaoui, M, Choukri, S & Shah, OR 2013, 'Dynamic characterisation of E-glass/epoxy composite behavior using SHPB techniques: tests and simulations', in *ICCM19*, July.
- Wang, J & Fu, J 2021 'Influence of water saturation on the strength characteristics and deformation behavior of hardened cement paste backfill', online published paper, viewed 10 February 2023, <https://doi.org/10.21203/rs.3.rs-351748/v1>
- Wu, D, Fall, M & Cai, SJ 2013, 'Coupling temperature, cement hydration and rheological behaviour of fresh cemented paste backfill', *Minerals Engineering*, vol. 42, no. 2, pp. 76-87, <https://doi.org/10.1016/j.mineng.2012.11.011>
- Yang, R, Li, W, Fang, S, Zhu, Y & Li, Y 2019, 'Experimental study on impact dynamic characteristics of layered composite rocks', *Chinese Journal of Rock Mechanics and Engineering*, vol. 38, no. 9, pp. 1747-1757.
- Zhang, M, Wu, H.J, Li, QM & Huang, FL 2009, 'Further investigation on the dynamic compressive strength enhancement of concrete-like materials based on split Hopkinson pressure bar tests', *Part I: Experiments. International Journal of Impact Engineering*, vol. 36, no. 12, pp. 1327-1334, <https://doi.org/10.1016/j.ijimpeng.2009.04.009>
- Zheng, D, Song, W, Cao, S & Li, J 2022, 'Dynamical mechanical properties and microstructure characteristics of cemented tailings backfill considering coupled strain rates and confining pressures effects', *Construction and Building Materials*, vol. 320, article no. 126321, <https://doi.org/10.1016/j.conbuildmat.2022.126321>
- Zheng, D, Song, W, Cao, S, Li, J & Sun, L 2021, 'Investigation on dynamical mechanics, energy dissipation, and microstructural characteristics of cemented tailings backfill under SHPB tests', *Minerals*, vol. 11, no. 5, article no. 542, <https://doi.org/10.3390/min11050542>
- Zvarivadza, T & Sengani, F 2018, 'Evaluation of the impact of production rate on mine seismicity: mechanised deep to ultra-deep level gold mining case study', in *52nd US Rock Mechanics/Geomechanics Symposium*, OnePetro, Richardson, paper no. ARMA-2018-681.